

See discussions, stats, and author profiles for this publication at: <https://www.researchgate.net/publication/336848038>

Hydrometeorological Monitoring Using Opportunistic Sensing Networks in the Amsterdam Metropolitan Area

Article in *Bulletin of the American Meteorological Society* · October 2019

DOI: 10.1175/BAMS-D-19-0091.1

CITATIONS

22

READS

315

8 authors, including:



Arjan Droste

TNO

12 PUBLICATIONS 112 CITATIONS

[SEE PROFILE](#)



Marjanne Zander

Deltares

4 PUBLICATIONS 72 CITATIONS

[SEE PROFILE](#)



Bert Heusinkveld

Wageningen University & Research

139 PUBLICATIONS 4,969 CITATIONS

[SEE PROFILE](#)



Gert-Jan Steeneveld

Wageningen University & Research

259 PUBLICATIONS 6,388 CITATIONS

[SEE PROFILE](#)

Some of the authors of this publication are also working on these related projects:



The Windy City [View project](#)



Weather Modelling [View project](#)



1 **Hydrometeorological monitoring using opportunistic sensing networks in**
2 **the Amsterdam metropolitan area**

3 L.W. de Vos^{*†}

4 *R&D Observations and Data Technology, Royal Netherlands Meteorological Institute (KNMI),*

5 *De Bilt, Netherlands*

6 *Hydrology and Quantitative Water Management Group, Wageningen University and Research,*

7 *Wageningen, Netherlands*

8 A.M. Droste[‡]

9 *Meteorology and Air Quality Section, Wageningen University and Research, Wageningen,*

10 *Netherlands*

11 M.J. Zander

12 *Hydrology and Quantitative Water Management Group, Wageningen University and Research,*

13 *Wageningen, Netherlands*

14 *Catchment and Urban Hydrology Department, Deltares, Delft, Netherlands*

15 A. Overeem

16 *R&D Observations and Data Technology, Royal Netherlands Meteorological Institute (KNMI),*

17 *De Bilt, Netherlands*

Early Online Release: This preliminary version has been accepted for publication in *Bulletin of the American Meteorological Society*, may be fully cited, and has been assigned DOI 10.1175/BAMS-D-19-0091.1. The final typeset copyedited article will replace the EOR at the above DOI when it is published.

18 *Hydrology and Quantitative Water Management Group, Wageningen University and Research,*
19 *Wageningen, Netherlands*

20 H. Leijnse

21 *R&D Observations and Data Technology, Royal Netherlands Meteorological Institute (KNMI),*
22 *De Bilt, Netherlands*

23 B.G. Heusinkveld

24 *Meteorology and Air Quality Section, Wageningen University and Research, Wageningen,*
25 *Netherlands*

26 G.J. Steeneveld

27 *Meteorology and Air Quality Section, Wageningen University and Research, Wageningen,*
28 *Netherlands*

29 R. Uijlenhoet

30 *Hydrology and Quantitative Water Management Group, Wageningen University and Research,*
31 *Wageningen, Netherlands*

32 * *Corresponding author address:* L.W. de Vos, Utrechtseweg 297, 3731 GA, De Bilt, Netherlands

33 E-mail: lotte.devos@wur.nl

34 † Contributed equally to this work with: A.M. Droste

35 ‡ Contributed equally to this work with: L.W. de Vos

ABSTRACT

36 The ongoing urbanisation and climate change urges further understanding
37 and monitoring of weather in cities. Two case studies during a 17-day period
38 over the Amsterdam metropolitan area, the Netherlands, are used to illus-
39 trate the potential and limitations of hydrometeorological monitoring using
40 non-traditional and opportunistic sensors. We employ three types of oppor-
41 tunistic sensing networks to monitor six important environmental variables:
42 (1) air temperature estimates from smartphone batteries and personal weather
43 stations; (2) rainfall from commercial microwave links and personal weather
44 stations; (3) solar radiation from smartphones; (4) wind speed from personal
45 weather stations; (5) air pressure from smartphones and personal weather
46 stations; (6) humidity from personal weather stations. These observations
47 are compared to dedicated, traditional observations where possible, although
48 such networks are typically sparse in urban areas. First we show that the pas-
49 sage of a front can be successfully monitored using data from several types
50 of non-traditional sensors in a complementary fashion. Also we demonstrate
51 the added value of opportunistic measurements in quantifying the Urban Heat
52 Island (UHI) effect during a hot episode. The UHI can be clearly determined
53 from personal weather stations, though UHI values tend to be high compared
54 to records from a traditional network. Overall, this study illustrates the enor-
55 mous potential for hydrometeorological monitoring in urban areas using non-
56 traditional and opportunistic sensing networks. (Capsule Summary) Several
57 opportunistic sensors (private weather stations, commercial microwave links
58 and smartphones) are employed to obtain weather information and success-
59 fully monitor urban weather events.

60 **1. Introduction**

61 Traditionally, hydrologists and meteorologists, scientists and practitioners alike, have relied
62 on dedicated measurement equipment in their research and operations. Such instruments are
63 typically owned and operated by governmental agencies. Installed and maintained according to
64 (inter)national standards, they offer accurate and reliable information about the state of environ-
65 ment we study, monitor and manage. Standard instruments are often based on novel measurement
66 techniques that originate in the research community and have been tested extensively during
67 dedicated field campaigns.

68
69 Unfortunately, the operational measurement networks available to the hydrometeorological
70 community today often lack the required spatial and/or temporal density for high-resolution
71 monitoring or forecasting of rapidly responding environmental systems. Apart from the high
72 installation and maintenance costs of such dedicated networks, it can be challenging, if not im-
73 possible, to install meteorological monitoring instruments according to the official requirements
74 in urban areas (Oke 2006).

75
76 Yet, sensors are omnipresent in our environment nowadays, often related to the rapid devel-
77 opment in wireless communication networks (e.g. McCabe et al. 2017; Balsamo et al. 2018;
78 Tauro et al. 2018; Zheng et al. 2018). To make use of such opportunistic sensors could be greatly
79 beneficial to (meteorological) science and environmental monitoring and management operations.
80 Opportunistic sensors are devices that were not installed with the intention to generate large-scale
81 observations, but can be used as such. They may not be as accurate or reliable as the dedicated
82 equipment we are used to, let alone meet official international standards. However, they are

83 typically available in large numbers and are often readily accessible online. Hence, combined
84 with smart retrieval algorithms and statistical treatment, opportunistic sensors may provide a
85 valuable complementary source of information regarding the state of our environment.

86
87 This article surveys recent opportunistic sensing techniques in meteorology, from (1) rainfall
88 monitoring using commercial microwave links (CML) from cellular communication networks,
89 via (2) crowdsourcing urban air temperature, pressure and solar radiation using smartphones to
90 (3) high-resolution urban monitoring of air temperature, pressure, humidity, wind speed, and
91 rainfall using personal weather stations (PWS). Other opportunistic sensing examples are: using
92 security cameras as rainfall indicators (Allamano et al. 2015), rainfall information from sensors
93 in driving cars (Rabiei et al. 2013), deriving the UHI from measurements of gradients of shallow
94 groundwater

95 citeBuik2004, using fiber-optic cables (Bense et al. 2016), using airplanes to measure upper-air
96 wind and temperature (de Haan 2011), using hot-air balloons to measure boundary-layer winds
97 (de Bruijn et al. 2016), smartphone anemometers (Hintz et al. 2017), or using networks of solar
98 panels for radiation monitoring. Muller et al. (2015); Zheng et al. (2018) provide excellent
99 overviews of past and ongoing projects making use of opportunistic sensing techniques, and
100 USAID (2013) showcases practical applications of crowdsourcing projects for agricultural
101 purposes in Africa. We limit ourselves to the presented techniques since these are relatively
102 established even in developing countries, discussed in detail in literature, and observe near the
103 Earth's surface.

104
105 We present a 17-day analysis for the Amsterdam metropolitan area, the Netherlands, where
106 these opportunistic sensors are employed in a complementary fashion, in particular to provide

107 detailed monitoring (both time series and spatially) of the passage of a front, as well as to
108 demonstrate the potential of opportunistic sensors to quantify the Urban Heat Island (UHI) effect.
109 This study aims to showcase the availability of several opportunistic sensing techniques and their
110 ability to capture meteorological events.

111

112 **2. Sampling techniques**

113 *a. Traditional sensing methods*

114 We use three traditional data sources as reference for the opportunistic sensing observations: a
115 gauge-adjusted radar product; the WMO station at Amsterdam airport; and the Amsterdam Atmo-
116 spheric Monitoring Supersite (AAMS (Ronda et al. 2017)) urban network. Details on instrumen-
117 tation and processing of these datasets are provided in the Appendix.

118 *b. Opportunistic sensing methods*

119 1) SMARTPHONE DATA

120 Smartphones contain many sensors to support their functionality, including sensors for light
121 levels to adjust screen brightness, pressure sensors to complement the GPS for an accurate
122 (vertical) location estimation, and thermometers for the battery to avoid damage from overheating.
123 Readings from such sensors can be used for opportunistic environmental sensing by collecting
124 them through mobile applications ('apps'). These apps sample the sensor readings with a certain
125 frequency, along with the last stored GPS coordinates. Examples of apps that collect and store
126 smartphone sensor readings include PressureNet (<http://www.cumulonimbus.ca/>) (Mass and
127 Madaus 2014; Madaus and Mass 2017), OpenSignal (<https://opensignal.com/>), and Atmos

128 (Niforatos et al. 2014, 2017).

129

130 Mass and Madaus (2014); Madaus and Mass (2017); McNicholas and Mass (2018), show that
131 assimilating smartphone pressure data into NWP models improves representation of convective
132 events. Likewise, Hintz et al. (2019) show for a case in Denmark that assimilating smartphone
133 pressure observations decreased the surface pressure bias in a NWP model. Different quality
134 control methods were applied: for Madaus and Mass (2017) the raw smartphone pressure readings
135 were filtered to only include one value per smartphone per assimilation time step, and were also
136 corrected for the terrain elevation and checked for spatial and statistical consistency. Hintz et al.
137 (2019) additionally use a consistency check with synoptic observations. In McNicholas and
138 Mass (2018) a machine learning algorithm was used to remove outliers. Niforatos et al. (2017)
139 compared smartphone light sensor readings with manually reported classifications of weather,
140 which showed light readings to be indicative of present weather conditions.

141

142 City-wide air temperatures can be estimated from smartphone battery temperature readings, as
143 has been shown for eight major cities (Overeem et al. 2013b), for the city of Birmingham (Muller
144 et al. 2015) for daily temperatures, and for São Paulo for hourly and daily temperatures (Droste
145 et al. 2017). Statistical training with independent temperature measurements was performed based
146 on a steady-state heat transfer model: a smartphone is typically carried close to the user's body.
147 The thermal energy generated by the smartphone must be balanced by heat exchange to the body
148 and the environment. The conductive heat flow between two adjacent systems is assumed to
149 be proportional to their temperature difference, and depends on the thermal insulation between
150 smartphone and environment, and between smartphone and body. This principle allows us to
151 estimate hourly-averaged air temperatures from hourly-averaged battery temperatures (Overeem

152 et al. 2013b):

$$153 \quad \bar{T}_{e,j,h}^{A,\text{hour}} = m_j^h (\bar{T}_{\text{bat},j,h}^{A,\text{hour}} - T_0) + T_0 + \varepsilon_{j,h}, \quad (1)$$

154 where $\bar{T}_{e,j,h}^{A,\text{hour}}$ is the hourly mean urban air temperature, $\bar{T}_{\text{bat},j,h}^{A,\text{hour}}$ is the hourly-averaged battery
155 temperature (both in space A and time), and T_0 a constant equilibrium temperature. m_j^h is a
156 coefficient, $\varepsilon_{j,h}$ is a random disturbance, and h denotes the hour.

157
158 In this study we build upon a large dataset of observations obtained from the Android appli-
159 cation OpenSignal, which crowdsources data relevant to wireless connectivity along with the
160 aforementioned sensor readings. Compared to the previously mentioned studies, readings were
161 obtained at a far higher frequency, i.e. 15-s intervals whenever the smartphone screen is active,
162 not requiring the app to be opened by the user. A total of 3.14 million smartphone observations
163 are available for the entire study period for the Amsterdam metropolitan region (larger domain in
164 Figure 1a).

165
166 The OpenSignal dataset includes self-reported accuracy scores (1, 2 or 3) of the light and
167 pressure readings, as determined by the sensor management software in the smartphones (Android
168 2019). Only readings with the highest possible accuracy were included in our analysis. All
169 smartphone pressure sensor readings below 950 hPa are excluded, based on the lowest recorded
170 pressure in the Netherlands, 954.2 hPa (de Haij 2009), which results in a dataset of 2.06 million
171 pressure readings. Light sensor readings above 0 lux are taken into account, leaving 2.32 million
172 light readings in the whole study period. We only include battery temperature readings between
173 10 – 47°C when the smartphone is not charging: 0.4 million temperature readings within the city
174 center. Hourly battery temperature readings are averaged spatially over the city center domain

175 (Figure 1b), light and pressure are averaged over the entire region for each hour (Figure 1a).

176

177 Ambient air temperatures are estimated from battery temperature (Eq. 1); the value of equilib-
178 rium temperature (T_0) as optimized by Overeem et al. (2013b), 39°C, is used. Figure 1b shows
179 the positions of the underlying battery temperature readings. Two different datasets are derived:
180 one without and one with optimizing the coefficients of the heat transfer model for the available
181 dataset. The first dataset uses a fixed value of m_j^h for all hours, 2.4, as found for a summer period
182 in London based on daily averages (Overeem et al. 2013b). These results, without further model
183 calibration, are presented in Figure 2b, which also shows the 25th and 75th percentile. For the
184 second dataset, records from 1 June 00:00 UTC –15 June 00:00 UTC are employed to calibrate a
185 value of m_j^h for each clock-hour (24 in total, ranging between 2.0 to 2.6). These optimized values,
186 found using a least squares regression, are applied to the validation dataset from 16 June 00:00
187 UTC – 23 June 00:00 UTC.

188

189 A smartphone light sensor measures illumination in lux (lumen m^{-2}), i.e. irradiance weighted
190 for the visible part of the electromagnetic spectrum, so a measure for the perceived brightness for
191 the human eye. To estimate the equivalent solar radiation, we use an empirical factor of 0.0079
192 lux per W m^{-2} , based on the spectral distribution of sunlight (Chua 2009). By applying this
193 transformation, the readings are treated as if they were measurements of solar radiation. This is
194 a fairly strong assumption, as we expect that most readings will not be made in a representative
195 manner: with the smartphone perpendicular towards the Sun and in direct sunlight. User behavior
196 plays a large role (e.g. indoor versus outdoor measurements), so one may expect that most light
197 readings will underestimate the solar radiation, resulting in a skewed distribution. A light sensor
198 in a smartphone has a limited view angle ($<180^\circ$) and has a relatively poor cosine response.

199 Additionally, the sensor can over-saturate at high light intensities (the sensor limit is typically
200 around 200 W m^{-2}). Therefore it is desirable to have many readings to increase the probability of
201 observations taken in favorable conditions (unshaded and perpendicular to direct sunlight).

202

203 Because smartphone measurements are taken when the smartphone is used, most data is
204 available for those times where people are active. Since hundreds of smartphone measurements
205 are required to obtain a good signal of air temperature (Droste et al. 2017), spatial detail is limited
206 to Local Climate Zone (LCZ, (Stewart and Oke 2012)) scale at best, and temporal resolution to
207 roughly hourly. The data at this availability is useful to get a broad overview of urban temperature,
208 but not for (spatially) detailed studies.

209

210 2) COMMERCIAL MICROWAVE LINKS

211 Cell phone communication relies on a telecommunication link network that consists of transmit-
212 ting and receiving antennas, typically several km apart, between which radio signals propagate.
213 Telecom operators commonly use signal frequencies that are sensitive to hydrometeors. This
214 causes attenuation of the microwave link signals when liquid precipitation occurs between the
215 antennas. Upton et al. (2005) first suggested to use signal attenuation in CML networks, which
216 is typically monitored for quality control purposes, to determine rainfall. Soon after, this was
217 shown to be successful with actual CML data (Messer et al. 2006; Leijnse et al. 2007). This was
218 promising as microwave link networks are widespread, also in areas of the world with limited
219 to no traditional rainfall sensors. Subsequent research has focused on improving the techniques
220 to obtain accurate rainfall estimates from these datasets, (e.g. Leijnse et al. 2008; Zinevich et al.
221 2010; Overeem et al. 2011; Chwala et al. 2012) and produce rainfall maps (Overeem et al. 2013a,

222 2016b) with real-time applicability (Chwala et al. 2016; Andersson et al. 2017; Chwala et al.
223 2018). Comprehensive overviews of literature on this technique were provided by Messer and
224 Sendik (2015), Uijlenhoet et al. (2018), and Chwala and Kunstmann (2019). Several tools have
225 been developed, documented and made (freely) available for users to construct rainfall obser-
226 vations with CML data: ‘Rcmlrain’ (<https://github.com/fenclmar/Rcmlrain>), ‘RAIN-
227 LINK’ (<https://github.com/overeem11/RAINLINK>), ‘pycomlink’ (<https://github.com/pycomlink/pycomlink>), and ‘pySNMPdaq’ (<https://github.com/cchwala/pySNMPdaq>).

229

230 The relation between rainfall attenuation and rainfall intensity can be described with a power law
231 between path-averaged specific signal attenuation (k in dB km^{-1}) and link path-averaged rainfall
232 intensity (R in mm h^{-1}) (Atlas and Ulbrich 1977):

$$R = ak^b \quad (2)$$

233 where

$$A = \text{TSL} - \text{RSL}; \quad k = \frac{A_{\text{wet}} - A_{\text{dry}} - A_a}{L} \quad (3)$$

234 Coefficients a (in $\text{mm h}^{-1} \text{dB}^{-b} \text{km}^b$) and b (-) are dependent on signal frequency and
235 polarization (Olsen et al. 1978; Jameson 1991). TSL and RSL are the transmitted and received
236 signal level (dB) respectively, A_a is the attenuation due to wet antennas (dB) assumed as a fixed
237 value, A_{wet} and A_{dry} are the attenuation under wet and dry weather conditions respectively (dB)
238 and L is the length of the link path (km). The specific attenuation due to rainfall is what remains
239 when the attenuation due to other causes (i.e. dry weather conditions and wet antennas) are

240 subtracted.

241

242 The time series shown in Figure 2d originate from the T-Mobile CML network visualized in
243 Figure 1a. Between 6 June 00:00 UTC and 10 June 14:00 UTC, 74 links were operational in
244 the study area. Power levels were instantaneously sampled every 15 min. Due to data transfer
245 issues, no power levels were available at the end of the study period. Rainfall time-series for each
246 link were constructed with the open source package RAINLINK (Overeem et al. 2016a), using
247 the approach and optimized parameters from (de Vos et al. 2019b). The wet antenna attenuation
248 makes up a larger fraction of the total attenuation for short links, meaning that a small error in A_a ,
249 a constant, will result in a relatively large error in k for short links, and the effect on the estimated
250 value of R would subsequently be larger than for long links given the same error in A_a .

251

252 3) CROWDSOURCED PERSONAL WEATHER STATIONS

253 PWSs allow anyone to measure weather variables in their direct environment. Many automatic
254 PWSs can upload their measurements directly to online platforms where they can be visualized
255 and shared. Weather Underground (<https://www.wunderground.com/wundermap>), WOW-NL
256 (<https://wow.knmi.nl/>) and the Netatmo Weathermap (<https://weathermap.netatmo.com/>)
257 are examples of platforms where weather observations are visualized in real time. Ideally,
258 weather variables can be crowdsourced from such platforms in far higher spatial and temporal
259 resolution than from traditional sensor networks.

260

261 The devices are often low-cost with a lower expected measurement accuracy than typical
262 sensors from meteorological institutes. The PWSs are installed by citizens without expert

263 knowledge on sensor placement requirements and/or lacking available measurement site without
264 interference from surroundings. Hence we expect that many of the PWSs generate compromised
265 measurements. For tipping bucket rain gauges, obstructions (e.g. insects, twigs) and the device not
266 being completely level with the ground, could hinder the tipping mechanism. A shielded location
267 will also lead to underestimation of rainfall. Overestimation of rainfall can result from PWS
268 owners cleaning or handling the device, resulting in tipping bucket tips, creating measurements
269 of artificial rain. PWS wind measurements are also largely affected by their position in relation
270 to obstacles and the shielding effect of buildings. Furthermore, PWSs with a sonic anemometer
271 are sensitive to rain blocking the path of the sound waves, so data quality might be compromised
272 during rain events. Urban wind is highly variable in space, and is often measured as profile using
273 e.g. LIDAR (Drew et al. 2013), so spatial averaging of PWS wind measurements is needed to
274 obtain useful data. Temperature readings are highly affected by direct radiation: the lack of a
275 proper radiation screen in most PWSs can result in overestimation of temperature by several
276 degrees when positioned in direct sunlight (Bell et al. 2015; Chapman et al. 2017). Finally, the
277 updates of measurements to the platform can be infrequent, and connectivity problems will result
278 in large gaps in the time series.

279

280 Only a few studies compared PWSs with high-end sensors; temperature, relative humidity,
281 radiation, pressure, rainfall, wind speed and direction: Jenkins (2014); Bell et al. (2015),
282 temperature: Meier et al. (2015), rainfall: de Vos et al. (2017). Other studies have benefited
283 from available PWS temperature records in cities. The UHI is then defined as the difference
284 between PWS temperatures and a rural reference station (Meier et al. 2017; Chapman et al. 2017;
285 Fenner et al. 2017; Golroudbary et al. 2018; Napoly et al. 2018). Preliminary work has been
286 performed on crowdsourced wind (Droste et al. 2018) and rainfall measurements (de Vos et al.

287 2017; Golroudbary et al. 2018; Chen et al. 2018) (and explored with simulated PWS rainfall
288 measurements by de Vos et al. (2018) as well). In other studies code has been developed and made
289 available to apply quality control on crowdsourced PWS data (the CrowdQC R-package for PWS
290 temperature observations <https://depositonce.tu-berlin.de//handle/11303/7520.3>
291 and TITAN <https://github.com/metno/TITAN/> , and code to filter crowdsourced rainfall
292 observations PWSQC <https://github.com/LottededeVos/PWSQC>).

293
294 Measurements from all personal weather stations from the brand Netatmo in the Amsterdam
295 study area (Figure 1a) are evaluated. All devices measure temperature, pressure and humidity.
296 Additionally, rain and/or wind are measured in case those optional modules are installed for that
297 PWS. In order to standardize the variable time intervals, all measurements are attributed to the
298 timestamp of the 5-min interval in which it occurred. If multiple measurements occurred within
299 the 5-min interval they are averaged (or accumulated in case of rainfall). The measurements over
300 the study period are shown in Figure 2 (panels (a), (c), (f) and (h)), where panel (i) indicates the
301 dewpoint depression (*DPD*) as calculated from the temperature and humidity measurements from
302 the PWS. No QC treatment is applied on the PWS data to showcase the raw potential. *DPD* is here
303 preferred over dewpoint temperature itself to identify the frontal passage.

304 **3. Case selection & study area**

305 We selected Amsterdam (capital of the Netherlands) and its surroundings and the period
306 between 6 June 2017 00:00 UTC and 23 June 2017 00:00 UTC as case study period (local time is
307 UTC+2 hours). This period contains both sufficient data from opportunistic sensing techniques,
308 and interesting meteorological events to illustrate the potential of the opportunistic sensing
309 techniques. The selected region is bound by 4.67–5.05°E & 52.24–52.44°N (26 km × 22 km).

310 To be able to distinguish between the inner city and suburbs, the study area was divided into
311 two parts, i.e. the urban center dataset: 4.83–4.95°E. & 52.34–52.38°N and the suburban dataset
312 4.67–5.05°E. & 52.24–52.44°N, excluding the urban center area (Figure 1a).

313

314 The Netherlands has a temperate maritime climate (Köppen Cfb). With a mean temperature
315 of 18.0°C and 50.5 mm of rainfall June 2017 was about 2.5°C warmer and 10.5 mm drier than
316 the climatological mean (based on the past 30 years of observations at station WMO 06240
317 Amsterdam airport, henceforth referred to as "Amsterdam airport"). The month had eight summer
318 days and two tropical days (max. temp. above 25 & 30°C respectively).

319

320 On June 6, a small low-pressure system developed over the North Sea off the coast of the
321 Netherlands and passed over the country, resulting in a substantial pressure drop to 992 hPa, an
322 hourly maximum wind speed of 54 km h⁻¹ (7 Bft) and 12 mm of rainfall measured at Amsterdam
323 airport. In the morning of June 9, an active cold front brought in relatively cold air which resulted
324 in 27 mm of rainfall. A clear-sky episode occurred 9–11 June, while another cold front passed
325 in the early morning of June 12 (Figure 2i). In the following period, no rainfall occurred, and
326 temperatures were mild (daily maximum temperatures below 25°C), followed by a warm episode
327 between June 16 and June 19. On June 19 the maximum air temperature reached 29.8°C at
328 Amsterdam airport. This warm episode ended with the passage of a cold front and associated
329 rainfall and thunderstorms on June 22. For the remainder of the paper we will focus on two cases,
330 i.e. case A, describing the passing front and resulting rainfall at the start of the study period, and
331 case B, containing the hot summer period, with a focus on UHI detection.

332

333 For this study, the UHI is defined as the instantaneous urban air temperature difference between
334 the city and the countryside (Stewart 2011). The UHI develops as a result of the relatively low
335 albedo of cities, high heat capacity of the urban fabric, thermal radiation trapping, and low surface
336 evapotranspiration. The UHI is favored by weather conditions with high solar insolation (low
337 cloud cover) and low wind speeds (Oke 1982; Theeuwes et al. 2017). Earlier crowdsourcing
338 observations indicated that Dutch urban areas experiences a mean daily maximum UHI of 2.3°C
339 and the 95th percentile amounts to 5.3°C (Steenefeld et al. 2011). Ronda et al. (2017) found a
340 mean evening UHI of $\sim 1^\circ\text{C}$, and a maximum of 4.5°C in Amsterdam for the summer of 2015 as
341 a whole.

342 4. Results

343 a. Case A: Weather front

344 First we focus on the passage of a cold front over the study area on June 9. At 6:00 UTC the
345 operational model analysis provided by KNMI locates the frontal zone to the west of Amsterdam
346 (not shown), and by 12:00 UTC the front has passed the city. Prior to the frontal passage itself,
347 an upper air disturbance passed over Amsterdam between 3:00 and 4:00 UTC, bringing strong
348 convection and rainfall. Such frontal zones cause distinctive behavior in various meteorological
349 variables, which we expect to be distinguishable in the crowdsourced data (Figure 2).

350
351 The passage of the front is clearly visible in the observed *DPD* and the wind speed (Figure 3a).
352 The *DPD* steadily drops during the approach and passage of the cold front, reaching a minimum
353 of 1.4°C at 9:00 UTC. Between 10:00 and 11:00 UTC, when the front has passed, the *DPD*
354 increases again up to 6.8°C, indicating the cold and dry air mass brought in by the cold front.

355 Crowdsourced and reference wind speed steadily increase as the front passes (from 2 to over 4
356 km h^{-1}), before reaching its maximum (5 km h^{-1}) directly after the passage. The convection
357 associated with the upper air disturbance at around 3:00–4:00 UTC generates a strong peak in
358 the wind speed. Despite the unknown measurement setup of the PWS anemometers, the average
359 signal of all PWSs corresponds well to that of the quality-controlled reference AAMS network
360 (mean bias of 0.4 km h^{-1}), which shows the same behavior for the upper air disturbance and the
361 front passing. However, the AAMS signal indicates a delayed onset of the wind speed increase (at
362 around 9:00 UTC) and takes longer to reach a higher maximum wind speed.

363

364 The ambient air pressure (Figure 3b), measured by PWSs and smartphones, starts increasing
365 at the moment the front passes (8:00 UTC). Typically, air pressure decreases before a cold front,
366 rapidly increases during the passage, and increases at a slower rate afterwards. The expected drop
367 prior to the frontal passage is not very pronounced in the measurements: there is a slight decrease
368 in pressure between 0:00 and 2:00 UTC (1.7 hPa decrease for PWS; 3.5 hPa for smartphone).
369 The latter is more likely associated with the upper air disturbance. After the frontal passage at
370 8:00 UTC, the pressure rises, from 1006–1008 hPa (PWS–smartphone) up to a maximum of
371 1013–1016 hPa at midnight. The pressure tendency remains roughly 1 hPa hour^{-1} after the front
372 has passed.

373

374 The light intensity as measured by smartphones shows a distinct diurnal pattern in Figure 2e,
375 following the course of solar radiation. The measured data are strongly skewed, so the median
376 light intensity values are low (Figure 2e). Figure 4 shows the 99th percentile of light readings to
377 capture the readings made in the most favorable light conditions (see Section 2.b.1). The sky on
378 June 9 is overcast (8 octas) until 11:00 UTC, at which time the front has passed over Amsterdam

379 and the sky clears up to scattered cloudiness (Figure 4). The light intensity is also very low until
380 10:00 UTC, even though this is well within daylight hours. Compared to June 18 (a clear day)
381 the light intensity is roughly halved, and the shape of the line is not as symmetrical (as we would
382 expect from the diurnal cycle of global radiation). The green lines in Figure 4 indicate the other
383 days over the study period, showing the strong variability in the daily course of light intensity.
384 The light intensity measured by smartphones not only depends on incoming radiation, but also
385 strongly on user behavior (indoors vs outdoors, the angle of the phone) and the type of light sensor
386 in the smartphone, which can differ between brands. The light sensor may also be oversaturated
387 during high light intensities, resulting in flattened peak values.

388
389 The light intensity peak at 4:00 UTC coincides with the the upper air disturbance seen
390 in Figure 3, but is actually an artifact of the low number of observations. The number of
391 available observations is higher during the day than during night and early morning, since it
392 is related to user activity whether the smartphone logs an observation (as detailed in Section
393 2.b.1). At 4:00 UTC there are only 502 smartphone observations, compared to 10,373 at 15:00
394 UTC (17:00 local time, the typical end of the working day), so the data is more sensitive to outliers.

395
396 The upper air disturbance, and subsequent frontal passage, of June 9 results in 27 mm rainfall
397 as measured by the gauge-adjusted radar reference. Figures 2c and 2d show that the peak of
398 rainfall occurs after sunrise, coinciding with the timing of the frontal passage. Figures 5a and
399 5b depict the cumulative rain over June 9, measured by CML and PWS, against the reference.
400 Total amounts differ between the two methods, but both show the same time response. The
401 relatively short links (< 2 km) overestimate rainfall, with the majority reporting > 30 mm rainfall
402 (relative bias is 87%). The longer links (≥ 2 km) also tend to overestimate, but much less

403 extreme (relative bias is 12%). Although the expected uncertainty in rainfall estimates is higher
404 for short links, the larger systematic bias (54% relative bias, or 0.13 mm absolute bias, for all
405 links) indicates that the methods to derive rainfall (RAINLINK) were not ideal for this rainfall
406 event, especially for short links.

407

408 PWS measurements tend to underestimate the rain as measured by the reference, with some
409 occurrences of large reported rainfall values that are not otherwise captured (Figure 5b). Never-
410 theless, the majority of PWSs seem to agree overall with the reference (Figures 5b and d). The
411 spatial distribution of rainfall (Figure 6) measured by PWS and CML corresponds to that of the
412 gauge-adjusted radar reference. We find that areas with high rainfall in the reference also yield
413 high accumulations in the CML and PWS data in these areas. The overestimation by short links
414 up to 8 mm is visible to the northwest of the band with high rainfall. The rainfall observations by
415 PWSs correspond well to the spatial pattern of rain, although a number measure little (< 1 mm)
416 rain during the hour represented in Figure 6. These stations are mainly clustered in the city center.
417 The large amount of obstructions inside the city center could reduce the rainfall received by the
418 stations, which may partly explain the underestimation tendency already seen in Figures 5b and d.

419

420 *b. Case B: Urban Heat Island*

421 The last days of the study period are characterized by high temperatures and generally clear,
422 sunny weather, leading to higher urban temperatures (PWS median air temperature up to 30°C on
423 June 19, Figure 7). Air temperature is measured by PWS, and derived through the smartphone
424 battery temperature using the second, calibrated dataset (Section 2.b.1). The AAMS network
425 serves as urban reference, and the Amsterdam airport measurements are used as rural reference

426 for the UHI (Figure 7b). The smartphone-derived air temperature differs clearly from the PWS
427 and AAMS measurements, with more erratic behavior and strong minimum values at night and
428 early morning (as low as 7°C when the AAMS values are above 16°C). Figure 7c showcases this
429 larger spread, also indicated by the large standard deviation (2.82 °C compared to 0.66 and 1.08
430 °C for the PWS). During daytime the smartphone-derived temperatures correspond better with the
431 PWS and AAMS measurements than at night. The diurnal cycle is clearly visible: the low values
432 at night are most likely due to a low number of measurements available, increasing the sensitivity
433 to outliers. Despite these occasional large deviations, the bias amounts to -0.6°C compared to
434 AAMS (Figure 7c), which is relatively small. A large positive bias (2.0°C) is found when a fixed
435 literature value for m_j^h is used, for the time series shown in Figure 2b, whereas the other model
436 statistics are mostly uninfluenced by optimizing m_j^h .

437
438 The diurnal pattern of air temperature between center and suburban PWSs is similar, although
439 the center stations tend to be warmer at night, and colder during the day (Figure 7a). The suburban
440 stations contain a higher spread and bias than the center stations, though both show good
441 agreement to the reference (Figure 7c). The AAMS air temperature is typically about 2 to 3°C
442 lower during the day: this could partially be caused by the unknown setup of the Netatmo station,
443 which is likely be exposed to direct sunlight or close to walls, making it sensitive to radiation
444 errors. Figure 7b depicts the UHI estimated by subtracting the center and suburban PWS (red
445 dashed line). This particular PWS–UHI shows spatial variability within the PWS data, which
446 is most pronounced during daytime, where the difference can be up to -1.5°C (i.e. the center is
447 1.5°C colder than the suburban area). Higher urban shading in the morning, and the faster heating
448 rate of the relatively thin rural boundary layer compared to the the deeper urban boundary layer

449 cause this urban cool island in the morning (Theeuwes et al. 2015).

450

451 The other two UHI estimates are constructed using Amsterdam airport as rural background,
452 showing that the city center is indeed much warmer at night than the rural surroundings. Urban
453 cool islands typically form in the morning, persisting for several hours before the city heats up
454 more. A remarkable 6°C UHI peak is visible on June 22, in the afternoon (13:00–14:00 UTC).
455 This seems to be mainly caused by the Amsterdam airport temperature, since the PWS–UHI
456 (which has no true rural reference) shows a value close to 0°C at that time. This is visible in
457 Figure 7a, where temperatures rapidly decrease in the course of a few hours on June 22 afternoon.
458 Thunderstorms were reported on this day, and several mm of rain were measured at Amsterdam
459 airport (according to radar) between 14:00 and 15:00 UTC. The UHI in this case is likely caused
460 by the sudden cooling of the rural reference, rather than strong urban heating.

461

462 Figure 8 presents the spatial variability in the AAMS and PWS temperature recordings between
463 2:00 and 3:00 UTC on June 18, when the UHI is typically largest. The cluster of stations in the
464 center yields higher values than the suburban stations, although in both areas many stations deviate
465 from this trend. The center PWS report an average UHI of 4.0°C, the AAMS UHI is 3.6°C,
466 whereas the suburban areas have an average UHI of 2.7°C. Variability between measurement
467 sites is high: some stations report a temperature difference of up to 12.4°C, and even a few with
468 negative UHI (up to -0.6°C).

469

470 **5. Discussion and conclusions**

471 *a. General*

472 We have shown that even though each technique has considerable limitations regarding accu-
473 racy, the data from opportunistic sources can be used to monitor meteorological phenomena. The
474 potential of these techniques lies in the high spatial density of such observations, especially in
475 urban areas.

476 We explicitly consider observations that can be obtained near-directly from the opportunist-
477 ic sensors, without applying many correction schemes, to illustrate their inherent potential:
478 validation using the available quality assurance schemes was not the aim of this research. We
479 use temperature from smartphone batteries and personal weather stations (PWS), rainfall from
480 commercial microwave links (CML) and PWS, solar radiation from smartphones, wind speed
481 from PWS, air pressure from smartphones and PWS, and humidity from PWS. Two case studies
482 in a 17-day period over the city of Amsterdam, the Netherlands, are explored. In the first case
483 study we show how the passage of a front is apparent from many of the data sources. The second
484 case study shows that these measurements can be valuable in monitoring the Urban Heat Island
485 (UHI) effect, especially given the fact that WMO stations in urban areas are very rare.

486
487 The passage of a cold front is visible in all of the studied opportunistic sensing data sources.
488 The dynamics of the temperature (especially from PWS, less so from smartphones), rainfall, solar
489 radiation, wind speed, air pressure, and humidity all show the passage of the front. However,
490 not every aspect of the weather events is sufficiently captured by the data: techniques using
491 smartphone observations can only estimate a variable as a spatial average over the city and cannot
492 be used to describe detailed spatial variability. Also, the PWS wind observations were too noisy

493 to describe spatial patterns in the city with confidence.

494

495 A rural reference station is needed to quantify the UHI, for which we use the WMO station
496 Amsterdam Airport. Even the PWS locations outside the city center of Amsterdam (suburban,
497 see Figures 1 and 8) are mostly in built-up areas, and are hence expected to experience the UHI,
498 although less severely. This is supported by Figure 7b, where the temperature difference between
499 the city center and the suburban areas is much less pronounced than when the WMO station is
500 used as rural reference. Using a single rural reference to quantify the UHI, instead of multiple
501 background stations, is a good practice when the main interest is in the intra-urban variability of
502 temperature, as in this work and e.g. Fenner et al. (2017). However, a limitation of this practice is
503 evident from the artificially high UHI we see in Figure 7 on June 22, which was caused by local
504 cooling at the rural site. Finally, we note that the distinction between center and suburban in this
505 study was made rather crudely. In future UHI studies we recommend a more sophisticated parti-
506 tioning of the stations into different classes (such as Local Climate Zones (Stewart and Oke 2012)).

507

508 *b. Temperature*

509 The PWSs are suitable for monitoring the UHI. When compared to the AAMS urban reference
510 network, these PWS show an UHI of the same order of magnitude (2–4°C), especially during
511 the night. We observe urban cool islands during the period between sunrise and local noon. Air
512 temperatures derived from smartphone battery temperatures exhibit much more noise than PWS
513 temperatures, which limits their use for UHI measurement. We note that the PWS thermometers
514 are not shielded from solar radiation or ventilated, whereas the AAMS are. This is clearly visible

515 in Figure 7, where the PWS temperature (and derived UHI) increases much more quickly than the
516 AAMS temperature. This corresponds to the findings of Bell et al. (2015).

517 *c. Pressure*

518 Both smartphones and PWSs provide good estimations of pressure. Pressure fields are relatively
519 constant in time and space, and both opportunistic sensing techniques show ability to describe
520 them.

521 *d. Light*

522 Light estimations derived from smartphones are highly variable in time. The indirect nature
523 of the measurement and the typical suboptimal conditions during sampling result in merely an
524 indicative observation of light. Such measurements should only be considered in the absence of
525 dedicated sensor observations and considered with caution.

526 *e. Wind*

527 Average wind speed from the PWSs are very low compared to what would be expected during
528 the passage of a front. This may partly be due to how the PWS anemometers are installed.
529 However, the carefully installed AAMS stations show average wind velocities of the same order
530 of magnitude (around 5 km h^{-1}), indicating that the placement of the anemometers does not play
531 a large role here. The reasons for these wind speeds to be lower than expected lies in the fact
532 that the urban wind measurements are made at a lower level, and the urban fabric greatly reduces
533 wind speeds at street level (Macdonald 2000). This also means that wind speeds are expected to
534 be highly variable across the city, which is clear from Figure 2f. Spatial averaging over the city is
535 therefore needed in order to see clear signals in the wind speed. Spatial averages of wind speed

536 show the same behavior between PWS and AAMS, indicating their use to measure the urban wind
537 as a whole. Note that the wind sensor on the Netatmo PWS is a sonic anemometer, which are
538 negatively affected by precipitation, hence wind observations during rainfall can be less reliable.
539 This illustrates the need of a quality-control procedure which could improve overall data quality
540 by filtering out precipitation events (Droste et al. 2018).

541

542 *f. Rainfall*

543 Data from PWS and CML are shown to provide useful information on both rainfall amount
544 and space-time variation. Their ability to show detailed variations in space and time makes them
545 useful for qualitative use in rainfall monitoring. The CML network overestimated rainfall in case
546 A (Figure 5a), although the relative bias of long links (≥ 2 km) was 71% smaller than that of
547 short links (< 2 km). This is likely related to the larger error contribution wet antennas have for
548 shorter links, and that the correction was calibrated on a different dataset, possibly with more long
549 links (de Vos et al. 2019b).

550

551 The PWS also show a good agreement with the reference, although most stations underestimate
552 rainfall (Figure 5b). This may be due to the higher wind speed above the urban fabric which could
553 cause buildings to act as a shield for the PWS rain gauges. It is also apparent from Figure 5d that
554 some PWSs report either zero rainfall when there is clearly rain or large amounts of rainfall where
555 there was none. Such, and other errors could be corrected by using automated filters (de Vos et al.
556 2019a). The difference in accumulations between the city-averaged CML and PWS rainfall data
557 (see Figure 2) is partly caused by the overestimation by CML. However, differences may also be
558 due to the spatial variation of rain and the respective locations of the PWS and CML. Figure 6

559 shows that for the examined hour the CML are more abundant in high-rainfall areas, whereas the
560 PWS are more clustered in the city center, where less rainfall was observed.

561

562 The method used to derive rainfall estimates from CML data (RAINLINK) is one of many
563 possible methods (see Section 2.b.2). Our dataset consists of instantaneously sampled CML data,
564 which is more prone to errors than CML data obtained with other sampling strategies and/or more
565 frequently than every 15 min (de Vos et al. 2019b).

566

567 *g. Outlook*

568 Our study shows that the research opportunistic sensing techniques all yield meaningful results.
569 However, without quality control procedures, PWS data performs better than smartphone or
570 CML measurements. The PWS sensors are designed to measure hydrometeorological variables
571 and are less reliant on quality control than the indirect CML or smartphone observations. A
572 thorough procedure which removes error sources will therefore be most effective for the CML
573 and smartphone data, which can strongly improve with regards to the unfiltered signal. This may
574 change in the future when the expected measurement density of smartphones increases and their
575 hardware (sensor capability) improves. The observations contain large errors, as found by the
576 larger spread in the data than would be explained by spatial or temporal variability. However, the
577 opportunistic sensors provide information in time scales and areas that cannot be achieved with
578 traditional sensing techniques.

579

580 Many PWSs are found in densely populated areas, where also many smartphones are opera-
581 tional. This is mainly true for urban areas in parts of the world where people have funds to invest

582 in these devices (although smartphones are considered so important that they are essentially
583 ubiquitous, independent of living standards). CML networks differ as well, in sampling strategy
584 and frequency (which affects the accuracy of rainfall estimates) and in network density (depending
585 on replacement by fiber optic technology). The availability of opportunistic sensing observations
586 should be explored in order to judge their usefulness, especially as their accuracy heavily relies
587 on the quantity of observations. Because traditional meteorological measurements are generally
588 absent in urban areas, these new data provide a welcome addition. This is particularly important
589 for monitoring the UHI, and wind and rainfall at street level. We therefore urge the scientific
590 community to keep investigating new sources of data, and to study the uncertainties therein. In
591 combination with reference networks of meteorological measurements or stand-alone, these new
592 sources will provide much needed hydrometeorological information for citizens and scientists, in
593 any part of the world.

594

595 *Acknowledgments.* Gert-Jan Steeneveld and Arjan Droste acknowledge funding from the Nether-
596 lands Organisation for Scientific Research (NWO) project 864.14.007. Lotte de Vos is financially
597 supported by KNMI MSO project 2013.09. The reference stations of the Amsterdam Atmospheric
598 Monitoring Supersite have been financially supported by the Amsterdam Institute for Advanced
599 Metropolitan Solutions (AMS), which has also provided co-funding (project VIR17006). We
600 thank James Robinson from OpenSignal (London, UK) for providing the smartphone dataset.
601 We gratefully acknowledge Ronald Kloeg and Ralph Koppelaar from T-Mobile NL for provid-
602 ing the cellular telecommunication link data. All PWS owners who have contributed to the Ne-
603 tatmo dataset are greatly appreciated, as well as the Netatmo company for making the measure-
604 ments available to us. See <https://dev.netatmo.com/resources/technical/reference/>

605 weatherapi/getpublicdata for information on how to obtain Netatmo data. Datasets re-
606 trieved from third parties (CML and OpenSignal) are available upon request. The gauge-adjusted
607 radar rainfall dataset is freely available in netCDF4 format, ‘Radar precipitation climatology’ via
608 <http://climate4impact.eu> or in HDF5 format at the KNMI Data Centre https://data.knmi.nl/datasets/rad_nl25_rac_mfbs_em_5min/2.0?q=radar. The AAMS data are
609 available upon request (contact: bert.heusinkveld@wur.nl).
610

611 APPENDIX

612 **Traditional sensing methods**

613 *a. Gauge-adjusted radar dataset*

614 The Royal Netherlands Meteorological Institute (KNMI) operates two C-band Doppler weather
615 radars. The 5-min reflectivity data from these radars are combined into one composite using a
616 weighing factor as a function of distance from the radar. Beekhuis and Mathijssen (2018) provide
617 detailed characteristics on the radars and the processing of their data. Reflectivity factors Z (mm^6
618 m^{-3}) are converted to rainfall intensities R (mm h^{-1}) with a fixed Z - R relationship (Marshall et al.
619 1955), $Z = 200R^{1.6}$, and, subsequently, accumulated to rainfall depths for different durations.
620 The two KNMI rain gauge networks are employed to adjust the radar-based accumulated rainfall
621 depths: an automatic network with 1-h rainfall depths for each hour (~ 1 station per 1000 km^2)
622 and a manual network with 24-h 08:00–08:00 UTC rainfall depths (~ 1 station per 100 km^2).
623 A daily spatial adjustment utilizing the manual gauge data is combined with an hourly mean-
624 field bias adjustment employing the automatic gauge data. The resulting gauge-adjusted radar
625 rainfall dataset has a spatial resolution of 0.9 km^2 , with no missing data for the study period.
626 Overeem et al. (2011) provide a more detailed description of this radar dataset, which largely uses

627 the methodology developed by Overeem et al. (2009a,b). Finally, 15-min path-averaged rainfall
628 intensities are derived from the radar pixels covering each link path of the CML dataset (described
629 in Section 3.b.2). The gauge-adjusted radar rainfall dataset is used as a reference to validate rainfall
630 estimates from CMLs and PWSs.

631 *b. WMO station Amsterdam airport*

632 The WMO station Amsterdam airport, WMO 06240 (4.78°E, 52.32°N; Figure 1a) provides
633 hourly air temperature and cloud cover observations. This surface synoptic station is operated by
634 KNMI, situated in a polder (4.18 m below MSL) and surrounded by meadows, arable land, and
635 buildings as well as infrastructure from Amsterdam airport. Air temperature is observed at 1.5-m
636 height above short mowed grass. The sensor is covered by a radiation screen and well ventilated.
637 Cloud cover aloft is obtained from a LD40 ceilometer, which uses LIDAR to detect the height and
638 concentration of particles, such as cloud droplets. KNMI (2000) provides more information on the
639 temperature observation.

640 *c. Amsterdam Atmospheric Monitoring Supersite*

641 As an urban reference network we utilize the observations from the Amsterdam Atmospheric
642 Monitoring Supersite (AAMS; Ronda et al. (2017)), which consists of 30 weather stations across
643 the city. The network consists of temperature and humidity sensors (Decagon VP-3, U.S.A.)
644 mounted inside a 184 mm aspirated radiation shield (Davis, U.S.A.). The ventilation fan is pow-
645 ered by 2 small solar panels mounted on top of the shield. The fans work at global radiation levels
646 $>100 \text{ W m}^{-2}$. The radiation screens are mounted onto lantern posts using a boom to mount the
647 center of the radiation screen 0.46 m away from the edge of the lantern post at a height of 4.0
648 m above ground level. The sonic anemometer (Decagon DS-2, U.S.A.) has an accuracy of 0.30

649 m s⁻¹) or 3% (whichever is larger). The anemometers were mounted above the radiation screens
650 0.50 m away from the lantern post edges and at heights of 4.30 m (from ground level to center of
651 the anemometer).

652 **References**

653 Allamano, P., A. Croci, and F. Laio, 2015: Toward the camera rain gauge. *Water Resources Re-*
654 *search*, **51 (3)**, 1744–1757, doi:10.1002/2014WR016298.

655 Andersson, J. C. M., P. Berg, J. Hansryd, A. Jacobsson, J. Olsson, and J. Wallin, 2017: Microwave
656 links improve operational rainfall monitoring in Gothenburg Sweden. *Proceedings of the 1st*
657 *International Conference on Environmental Science and Technology*, 1–4.

658 Android, 2019: Android developer guide for SensorManagement. Last accessed 2019-
659 01-29, last updated 2019-01-23, [http://developer.android.com/reference/android/hardware/
660 SensorManager.html#SENSOR_STATUS_ACCURACY_HIGH](http://developer.android.com/reference/android/hardware/SensorManager.html#SENSOR_STATUS_ACCURACY_HIGH).

661 Atlas, D., and C. W. Ulbrich, 1977: Path-and area-integrated rainfall measurement by microwave
662 attenuation in the 1–3 cm band. *Journal of Applied Meteorology*, **16 (12)**, 1322–1331.

663 Balsamo, G., and Coauthors, 2018: Satellite and in situ observations for advancing global earth
664 surface modelling: A review. *Remote Sensing*, **10 (12)**, 2038.

665 Beekhuis, H., and T. Mathijssen, 2018: From pulse to product, highlights of the upgrade project
666 of the Dutch national weather radar network. 960–965, doi:10.18174/454537, extended abstract
667 for ERAD2018 conference.

668 Bell, S., D. Cornford, and L. Bastin, 2015: How good are citizen weather stations? Addressing a
669 biased opinion. *Weather*, **70 (3)**, 75.

670 Bense, V. F., and Coauthors, 2016: Distributed temperature sensing as a downhole tool in hydro-
671 geology. *Water Resources Research*, **52** (12), 9259–9273, doi:10.1002/2016WR018869.

672 Chapman, L., C. Bell, and S. Bell, 2017: Can the crowdsourcing data paradigm take atmospheric
673 science to a new level? A case study of the urban heat island of London quantified using
674 Netatmo weather stations. *International Journal of Climatology*, **37** (9), 3597–3605.

675 Chen, A. B., M. Behl, and J. L. Goodall, 2018: Trust me, my neighbors say it’s raining out-
676 side: Ensuring data trustworthiness for crowdsourced weather stations. *Proceedings of the 5th*
677 *Conference on Systems for Built Environments*, ACM, 25–28.

678 Chua, S., 2009: Light vs. distance. URL [http://bccp.berkeley.edu/o/Academy/workshop_09/pdfs/](http://bccp.berkeley.edu/o/Academy/workshop_09/pdfs/InverseSquareLawPresentation.pdf)
679 [InverseSquareLawPresentation.pdf](http://bccp.berkeley.edu/o/Academy/workshop_09/pdfs/InverseSquareLawPresentation.pdf), University Lecture, Powerpoint Slides.

680 Chwala, C., F. Keis, and H. Kunstmann, 2016: Real-time data acquisition of commercial mi-
681 crowave link networks for hydrometeorological applications. *Atmospheric Measurement Tech-*
682 *niques*, **9** (3), 991–999.

683 Chwala, C., and H. Kunstmann, 2019: Commercial microwave link networks for rainfall observa-
684 tion: Assessment of the current status and future challenges. Accepted.

685 Chwala, C., G. Smiatek, and H. Kunstmann, 2018: Real-time rainfall from a country-wide net-
686 work of commercial microwave links in Germany. 265–265, doi:10.18174/454537, abstract for
687 ERAD2018 conference.

688 Chwala, C., and Coauthors, 2012: Precipitation observation using microwave backhaul links in
689 the alpine and pre-alpine region of Southern Germany. *Hydrology and Earth System Sciences*,
690 **16** (8), 2647–2661.

- 691 de Bruijn, E. I. F., S. de Haan, F. C. Bosveld, B. W. Schreur, and A. A. M. Holtslag, 2016:
692 Observing boundary-layer winds from hot-air balloon flights. *Weather and Forecasting*, **31** (5),
693 1451–1463, doi:10.1175/WAF-D-16-0028.1.
- 694 de Haan, S., 2011: High-resolution wind and temperature observations from aircraft tracked by
695 mode-s air traffic control radar. *Journal of Geophysical Research: Atmospheres*, **116** (D10),
696 doi:10.1029/2010JD015264.
- 697 de Haij, M., 2009: Automatische validatie van druk- en windwaarnemingen op het KNMI - een
698 verkenning. Tech. rep., 1– pp. URL <http://bibliotheek.knmi.nl/knmipubIR/IR2009-03.pdf>, in
699 Dutch.
- 700 de Vos, L. W., H. Leijnse, A. Overeem, and R. Uijlenhoet, 2017: The potential of urban rainfall
701 monitoring with crowdsourced automatic weather stations in Amsterdam. *Hydrology and Earth
702 System Sciences*, **21** (2), 765–777.
- 703 de Vos, L. W., H. Leijnse, A. Overeem, and R. Uijlenhoet, 2019a: Quality control
704 for crowdsourced personal weather stations to enable operational rainfall monitoring.
705 *Geophysical Research Letters*, **46** (0), doi:10.1029/2019GL083731, URL [https://agupubs.
706 onlinelibrary.wiley.com/doi/abs/10.1029/2019GL083731](https://agupubs.onlinelibrary.wiley.com/doi/abs/10.1029/2019GL083731), [https://agupubs.onlinelibrary.wiley.
707 com/doi/pdf/10.1029/2019GL083731](https://agupubs.onlinelibrary.wiley.com/doi/pdf/10.1029/2019GL083731).
- 708 de Vos, L. W., A. Overeem, H. Leijnse, and R. Uijlenhoet, 2019b: Rainfall estimation accuracy of
709 a nation-wide instantaneously sampling commercial microwave link network: error-dependency
710 on known characteristics. *Journal of Atmospheric and Oceanic Technology*, **forthcoming**, doi:
711 10.1175/JTECH-D-18-0197.1.

- 712 de Vos, L. W., T. H. Raupach, H. Leijnse, A. Overeem, A. Berne, and R. Uijlenhoet, 2018: High-
713 resolution simulation study exploring the potential of radars, crowdsourced personal weather
714 stations and commercial microwave links to monitor small-scale urban rainfall. *Water Resources*
715 *Research*, **54** (12), 10 293–10 312.
- 716 Drew, D. R., J. F. Barlow, and S. E. Lane, 2013: Observations of wind speed profiles over Greater
717 London, UK, using a Doppler lidar. *Journal of Wind Engineering and Industrial Aerodynamics*,
718 **121**, 98–105, doi:10.1016/j.jweia.2013.07.019.
- 719 Droste, A. M., B. G. Heusinkveld, D. Fenner, and G. J. Steeneveld, 2018: Crowdsourcing the
720 urban wind. *EGU General Assembly Conference Abstracts*, Vol. 21, 5671.
- 721 Droste, A. M., J. J. Pape, A. Overeem, H. Leijnse, G. J. Steeneveld, A. J. Van Delden, and R. Uij-
722 jlenhoet, 2017: Crowdsourcing urban air temperatures through smartphone battery temperatures
723 in São Paulo, Brazil. *Journal of Atmospheric and Oceanic Technology*, **34**, 1853–1866.
- 724 Fenner, D., F. Meier, B. Bechtel, M. Otto, and D. Scherer, 2017: Intra and inter local climate zone
725 variability of air temperature as observed by crowdsourced citizen weather stations in Berlin,
726 Germany. *Meteorologische Zeitschrift*, **26**, 525–547.
- 727 Golroudbary, V. R., Y. Zeng, C. M. Mannaerts, and Z. B. Su, 2018: Urban impacts on air temper-
728 ature and precipitation over the Netherlands. *Climate Research*, **75** (2), 95–109.
- 729 Hintz, K., H. Vedel, J. Muñoz-Gomez, and N. Woetmann, 2017: An Examination of the Quality
730 of Wind Observations with Smartphones. *EGU General Assembly Conference Abstracts*, EGU
731 General Assembly Conference Abstracts, Vol. 19, 19568, URL [http://adsabs.harvard.edu/abs/](http://adsabs.harvard.edu/abs/2017EGUGA..1919568H)
732 [2017EGUGA..1919568H](http://adsabs.harvard.edu/abs/2017EGUGA..1919568H).

- 733 Hintz, K. S., H. Vedel, and E. Kaas, 2019: Collecting and processing of barometric data from
734 smartphones for potential use in numerical weather prediction data assimilation. *Meteorological*
735 *Applications*, **0** (0), doi:10.1002/met.1805, URL [https://rmets.onlinelibrary.wiley.com/doi/abs/](https://rmets.onlinelibrary.wiley.com/doi/abs/10.1002/met.1805)
736 [10.1002/met.1805](https://rmets.onlinelibrary.wiley.com/doi/pdf/10.1002/met.1805), <https://rmets.onlinelibrary.wiley.com/doi/pdf/10.1002/met.1805>.
- 737 Jameson, A. R., 1991: A comparison of microwave techniques for measuring rainfall. *Journal of*
738 *Applied Meteorology*, **30** (1), 32–54.
- 739 Jenkins, G., 2014: A comparison between two types of widely used weather stations. *Weather*,
740 **69** (4), 105–110.
- 741 KNMI, 2000: *Handbook for the Meteorological Observation*. Koninklijk Nederlands Meteorolo-
742 gisch Instituut, 91–110 pp., available via [http://projects.knmi.nl/hawa/pdf/Handbook_H01_H06.](http://projects.knmi.nl/hawa/pdf/Handbook_H01_H06.pdf)
743 pdf.
- 744 Leijnse, H., R. Uijlenhoet, and J. N. M. Stricker, 2007: Rainfall measurement using radio
745 links from cellular communication networks. *Water Resources Research*, **43** (3), doi:10.1029/
746 2006WR005631.
- 747 Leijnse, H., R. Uijlenhoet, and J. N. M. Stricker, 2008: Microwave link rainfall estimation: Effects
748 of link length and frequency, temporal sampling, power resolution, and wet antenna attenuation.
749 *Advances in Water Resources*, **31** (11), 1481–1493, doi:10.1016/j.advwatres.2008.03.004.
- 750 Macdonald, R. W., 2000: Modelling the mean velocity profile in the urban canopy layer.
751 *Boundary-Layer Meteorology*, **97** (1), 25–45, doi:10.1023/A:1002785830512.
- 752 Madaus, L. E., and C. F. Mass, 2017: Evaluating smartphone pressure observations for
753 mesoscale analyses and forecasts. *Weather and Forecasting*, **32** (2), 511–531, doi:10.1175/
754 WAF-D-16-0135.1.

- 755 Marshall, J. S., W. Hitschfeld, and K. L. S. Gunn, 1955: Advances in radar weather. *Advances in*
756 *Geophysics*, Vol. 2, Academic Press, New York, 1–56.
- 757 Mass, C. F., and L. E. Madaus, 2014: Surface pressure observations from smartphones: A potential
758 revolution for high-resolution weather prediction? *Bulletin of the American Meteorological*
759 *Society*, **95** (9), 1343–1349, doi:10.1175/BAMS-D-13-00188.1.
- 760 McCabe, M. F., and Coauthors, 2017: The future of earth observation in hydrology. *Hydrology*
761 *and Earth System Sciences*, **21** (7), 3879–3914.
- 762 McNicholas, C., and C. F. Mass, 2018: Smartphone pressure collection and bias correction using
763 machine learning. *Journal of Atmospheric and Oceanic Technology*, **35** (3), 523–540, doi:10.
764 1175/JTECH-D-17-0096.1, URL <https://doi.org/10.1175/JTECH-D-17-0096.1>, [https://doi.org/](https://doi.org/10.1175/JTECH-D-17-0096.1)
765 [10.1175/JTECH-D-17-0096.1](https://doi.org/10.1175/JTECH-D-17-0096.1).
- 766 Meier, F., D. Fenner, T. Grassmann, B. Jänicke, M. Otto, and D. Scherer, 2015: Challenges and
767 benefits from crowd-sourced atmospheric data for urban climate research using Berlin, Ger-
768 many, as testbed. *ICUC9 - 9th International Conference on Urban Climate jointly with 12th*
769 *Symposium on the Urban Environment*.
- 770 Meier, F., D. Fenner, T. Grassmann, M. Otto, and D. Scherer, 2017: Crowdsourcing air temperature
771 from citizen weather stations for urban climate research. *Urban Climate*, **19**, 170–191.
- 772 Messer, H., and O. Sendik, 2015: A new approach to precipitation monitoring: A critical survey
773 of existing technologies and challenges. *IEEE Signal Processing Magazine*, **32** (3), 110–122,
774 doi:10.1109/MSP.2014.2309705.
- 775 Messer, H., A. Zinevich, and P. Alpert, 2006: Environmental monitoring by wireless communica-
776 tion networks. *Science*, **312** (5774), 713–713, doi:10.1126/science.1120034.

777 Muller, C. L., L. Chapman, S. Johnston, C. Kidd, S. Illingworth, G. Foody, A. Overeem, and R. R.
778 Leigh, 2015: Crowdsourcing for climate and atmospheric sciences: current status and future
779 potential. *International Journal of Climatology*, **35**, 3185–3203, doi:10.1002/joc.4210.

780 Napoly, A., F. Meier, T. Grassmann, and D. Fenner, 2018: Development and application of a
781 statistically-based quality control for crowdsourced air temperature data. *Frontiers in Earth Sci-*
782 *ence*, **6**, 118.

783 Niforatos, E., A. Vourvopoulos, and A. Langheinrich, 2017: Understanding the potential of
784 human-machine crowdsourcing for weather data. *International Journal of Human-Computer*
785 *Studies*, **102 (Supplement C)**, 54 – 68, doi:https://doi.org/10.1016/j.ijhcs.2016.10.002, special
786 Issue on Mobile and Situated Crowdsourcing.

787 Niforatos, E., A. Vourvopoulos, M. Langheinrich, P. Campos, and A. Doria, 2014: Atmos: a
788 hybrid crowdsourcing approach to weather estimation. *Proceedings of the 2014 ACM Interna-*
789 *tional Joint Conference on Pervasive and Ubiquitous Computing: Adjunct Publication*, ACM,
790 135–138, doi:10.1145/2638728.2638780.

791 Oke, T. R., 1982: The energetic basis of the urban heat island. *Quarterly Journal of the Royal*
792 *Meteorological Society*, **108**, 1–24, doi:10.1002/qj.49710845502.

793 Oke, T. R., 2006: Initial guidance to obtain representative meteorological observations at urban
794 sites. *World Meteorological Organization, Geneva*, **ION report 81**.

795 Olsen, R. L., D. V. Rogers, and D. Hodge, 1978: The aR^b relation in the calculation of rain
796 attenuation. *IEEE Transactions on Antennas and Propagation*, **26 (2)**, 318–329, doi:10.1109/
797 TAP.1978.1141845.

- 798 Overeem, A., T. A. Buishand, and I. Holleman, 2009a: Extreme rainfall analysis and estimation
799 of depth-duration-frequency curves using weather radar. *Water Resources Research*, **45**, doi:
800 10.1029/2009WR007869, w10424.
- 801 Overeem, A., I. Holleman, and A. Buishand, 2009b: Derivation of a 10-year radar-based cli-
802 matology of rainfall. *Journal of Applied Meteorology and Climatology*, **48**, 1448–1463, doi:
803 10.1175/2009JAMC1954.1.
- 804 Overeem, A., H. Leijnse, and R. Uijlenhoet, 2011: Measuring urban rainfall using microwave
805 links from commercial cellular communication networks. *Water Resources Research*, **47**, doi:
806 10.1029/2010WR010350, w12505.
- 807 Overeem, A., H. Leijnse, and R. Uijlenhoet, 2013a: Country-wide rainfall maps from cellular
808 communication networks. *Proceedings of the National Academy of Sciences*, **110** (8), 2741–
809 2745, doi:10.1073/pnas.1217961110.
- 810 Overeem, A., H. Leijnse, and R. Uijlenhoet, 2016a: Retrieval algorithm for rainfall mapping from
811 microwave links in a cellular communication network. *Atmospheric Measurement Techniques*,
812 **9** (5), 2425–2444, doi:10.5194/amt-9-2425-2016.
- 813 Overeem, A., H. Leijnse, and R. Uijlenhoet, 2016b: Two and a half years of country-wide rainfall
814 maps using radio links from commercial cellular telecommunication networks. *Water Resources*
815 *Research*, **52** (10), 8039–8065, doi:10.1002/2016WR019412.
- 816 Overeem, A., R. J. C. Robinson, H. Leijnse, G. J. Steeneveld, P. B. K. Horn, and R. Uijlenhoet,
817 2013b: Crowdsourcing urban air temperatures from smartphone battery temperatures. *Geophys-*
818 *ical Research Letters*, **40** (15), 4081–4085.

- 819 Rabiei, E., U. Haberlandt, M. Sester, and D. Fitzner, 2013: Rainfall estimation using moving cars
820 as rain gauges-laboratory experiments. *Hydrology and Earth System Sciences*, **17** (11), 4701–
821 4712.
- 822 Ronda, R. J., G. J. Steeneveld, B. G. Heusinkveld, J. Attema, and A. A. M. Holtslag, 2017: Ur-
823 ban finescale forecasting reveals weather conditions with unprecedented detail. *Bulletin of the*
824 *American Meteorological Society*, **98** (12), 2675—2688, doi:10.1175/BAMS-D-16-0297.1.
- 825 Steeneveld, G. J., S. Koopmans, B. G. Heusinkveld, L. W. A. van Hove, and A. A. M. Holtslag,
826 2011: Quantifying urban heat island effects and human comfort for cities of variable size and
827 urban morphology in the Netherlands. *Journal of Geophysical Research: Atmospheres*, **116**,
828 D20 129, doi:10.1029/2011JD015988.
- 829 Stewart, I. D., 2011: A systematic review and scientific critique of methodology in modern urban
830 heat island literature. *International Journal of Climatology*, **31**, 200–217, doi:10.1002/joc.2141.
- 831 Stewart, I. D., and T. R. Oke, 2012: Local climate zones for urban temperature studies. *Bulletin of*
832 *the American Meteorological Society*, **93** (12), 1879–1900, doi:10.1175/BAMS-D-11-00019.1.
- 833 Tauro, F., and Coauthors, 2018: Measurements and observations in the XXI century (MOXXI):
834 innovation and multi-disciplinarity to sense the hydrological cycle. *Hydrological Sciences Jour-*
835 *nal*, **63** (2), 169–196.
- 836 Theeuwes, N. E., G. J. Steeneveld, R. J. Ronda, and A. A. M. Holtslag, 2017: A diagnostic
837 equation for the daily maximum urban heat island effect for cities in Northwestern Europe.
838 *International Journal of Climatology*, **37**, 443–454, doi:10.1002/joc.4717.

839 Theeuwes, N. E., G. J. Steeneveld, R. J. Ronda, M. W. Rotach, and A. A. M. Holtslag, 2015: Cool
840 city mornings by urban heat. *Environmental Research Letters*, **10** (11), 114 022, doi:10.1088/
841 1748-9326/10/11/114022.

842 Uijlenhoet, R., A. Overeem, and H. Leijnse, 2018: Opportunistic remote sensing of rainfall using
843 microwave links from cellular communication networks. *WIREs Water*, e1289, doi:10.1002/
844 wat2.1289.

845 Upton, G. J. G., A. R. Holt, R. J. Cummings, A. R. Rahimi, and J. W. F. Goddard, 2005: Microwave
846 links: The future for urban rainfall measurement? *Atmospheric Research*, **77** (1), 300–312, doi:
847 10.1016/j.atmosres.2004.10.009.

848 USAID, 2013: Crowdsourcing Applications for Agricultural Development in Africa.
849 URL [https://www.agrilinks.org/sites/default/files/resource/files/Crowdsourcing{ }](https://www.agrilinks.org/sites/default/files/resource/files/CrowdsourcingApplicationsforAgriculturalDevelopmentinAfrica.pdf)
850 Applications{ }for{ }Agricultural{ }Development{ }in{ }Africa.pdf, 1–6 pp.

851 Zheng, F., and Coauthors, 2018: Crowdsourcing methods for data collection in geophysics: State
852 of the art, issues, and future directions. *Reviews of Geophysics*, **56**, 698–740.

853 Zinevich, A., H. Messer, and P. Alpert, 2010: Prediction of rainfall intensity measurement er-
854 rors using commercial microwave communication links. *Atmospheric Measurement Techniques*,
855 **3** (5), 1385–1402.

856 **LIST OF FIGURES**

857 **Fig. 1.** Map of Amsterdam metropolitan area and city center with locations of all sensor networks:
 858 Personal Weather Stations (PWS) and Commercial Microwave Links (CML) (a), and of
 859 smartphone battery temperature readings and Amsterdam Atmospheric Monitoring Super-
 860 site (AAMS) stations (b). 43

861 **Fig. 2.** Time series of opportunistic measurements of weather variables. PWS observations of tem-
 862 perature (a), cumulative rainfall (c), wind (f), pressure (g) and dewpoint depression calcu-
 863 lated from humidity and temperature (i), smartphone battery derived air temperature (b),
 864 light (e) and pressure (g). The colored areas indicate the interquartile range (IQR is mean
 865 25–75 percentile) of all observations at that time; lines show the median values, except for
 866 (b) where the line shows mean temperature. Shaded areas indicate night-time. Pearson cor-
 867 relation (r), standard deviation of the difference (SD) and absolute bias (bias) are calculated
 868 based on hourly values compared with WMO observations at Schiphol. 44

869 **Fig. 3.** (a) Hourly average wind speed measured by PWS (solid line) and AAMS (dotted line),
 870 as well as the PWS dewpoint depression (red line, right y-axis). (b) Hourly averaged air
 871 pressure measured by PWS (solid line) and smartphone (dashed line) on June 9. The vertical
 872 lines indicate the boundaries of the frontal passage. At 6 UTC the front is located to the west
 873 of Amsterdam; at 12 UTC the front has passed over the city. 45

874 **Fig. 4.** Hourly 99th percentile of smart phone radiation (green lines) with Amsterdam airport cloud
 875 cover in oktas on June 9 (blue, circles) and June 18 (orange, diamonds). June 9 (blue solid
 876 line) and June 18 (orange solid line) are a cloudy and cloud-free day, respectively. 46

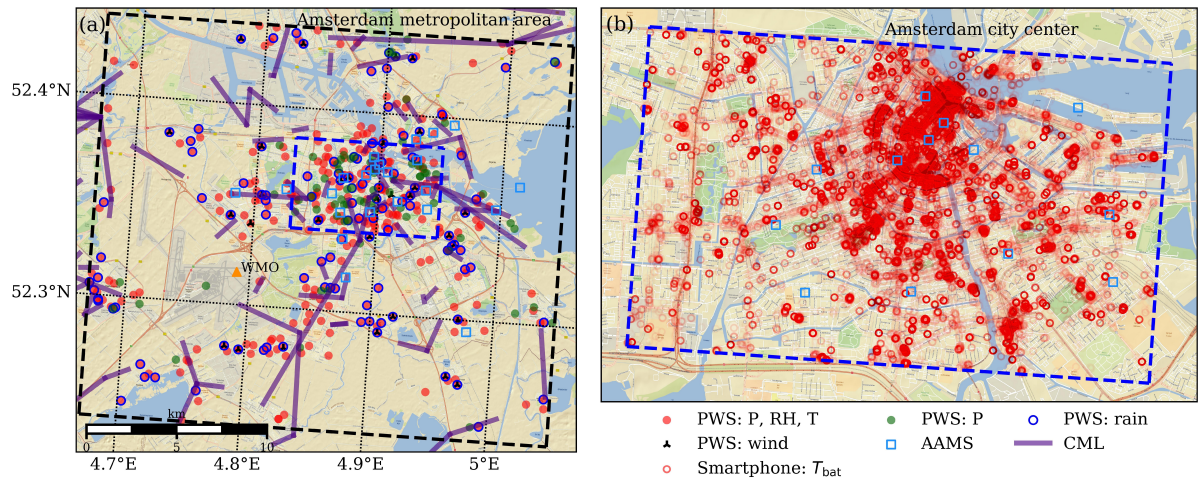
877 **Fig. 5.** Double mass plots of commercial microwave link derived rainfall observations (a) and PWS
 878 rainfall observations (b) on 9 June against the reference of respectively the path-averaged
 879 and overlying pixel gauge-adjusted radar rainfall observations. Polarization, path length and
 880 frequency of the CML network is given in (c) and (d) shows scatter plots of both together
 881 with their Pearson correlation (r), standard deviation of the difference (SD) and absolute
 882 bias (bias) at 15 min time steps. 47

883 **Fig. 6.** Map of 60-min rainfall depths over the Amsterdam metropolitan area based on gauge-
 884 adjusted radar data (pixels; 100% availability), CML data (paths; only CMLs with 100%
 885 availability are shown), and PWS data (circles; only PWSs with at least 83.3% availability
 886 are shown). 48

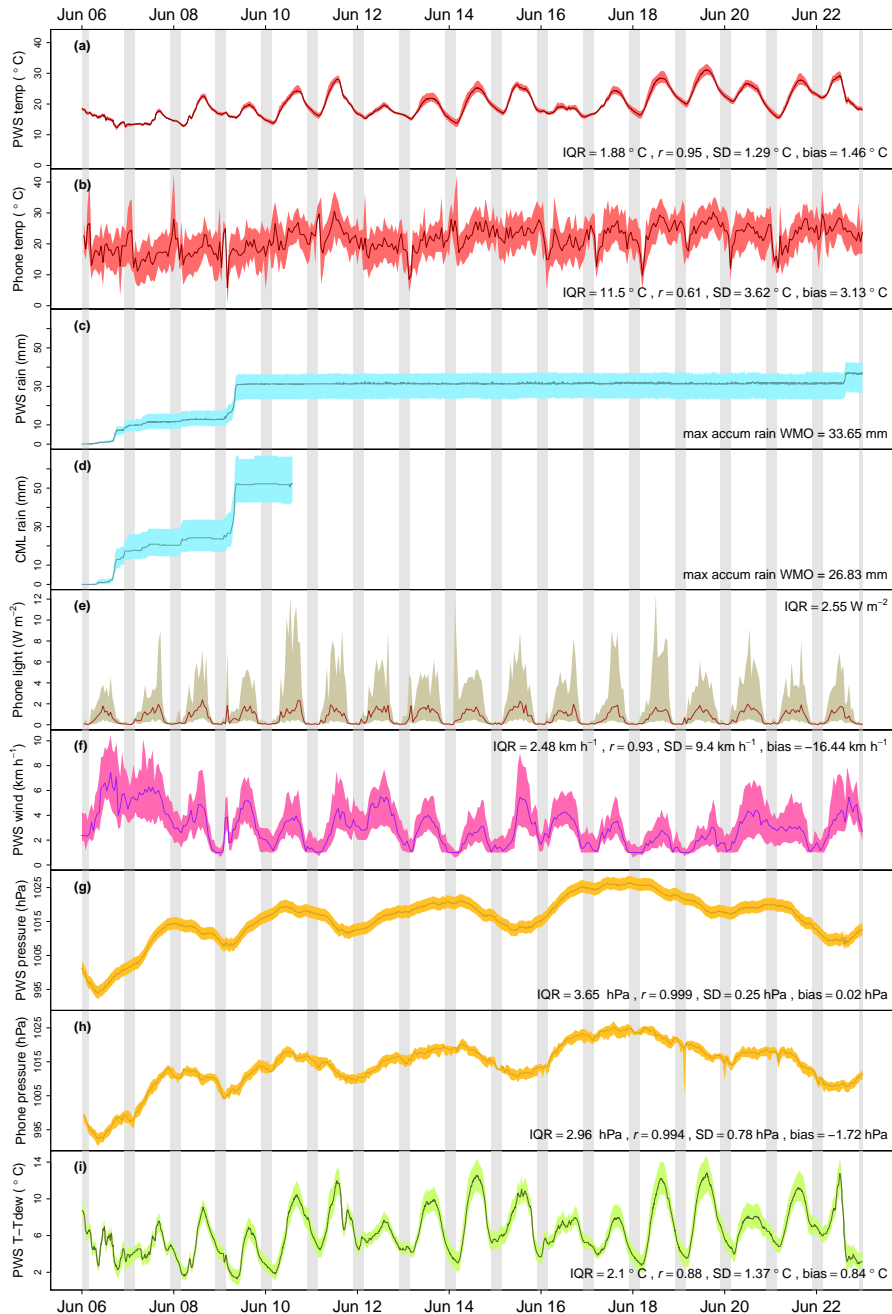
887 **Fig. 7.** (a) Time series of temperature measurement according to the median of all (blue), center
 888 (red) and suburban (green) PWSs, as well as the median of the AAMS network (orange)
 889 and the mean smartphone derived air temperatures (purple). (b) The difference between
 890 the median PWS center and suburban temperatures (red, dashed); the AAMS and WMO
 891 (blue, dashed); and the PWS center and WMO (green, dashed). Shaded areas indicate night-
 892 time. (c) Scatter plot of hourly median PWS and smartphone temperatures against median
 893 AAMS station data, with Pearson correlation (r), standard deviation of the difference (SD)
 894 and absolute bias (bias). 49

895 **Fig. 8.** Urban Heat Island map for the Amsterdam metropolitan area (black rectangle) showing
 896 difference between hourly averaged air temperature for AAMS network (squares) and PWSs
 897 (circles) with respect to 1.5-m air temperature at WMO station Amsterdam airport observed
 898 at 3 UTC (triangle). The blue rectangle represents Amsterdam city center, the remainder of
 899 the metropolitan area is suburban. Only stations with at least 80% availability are shown. Of

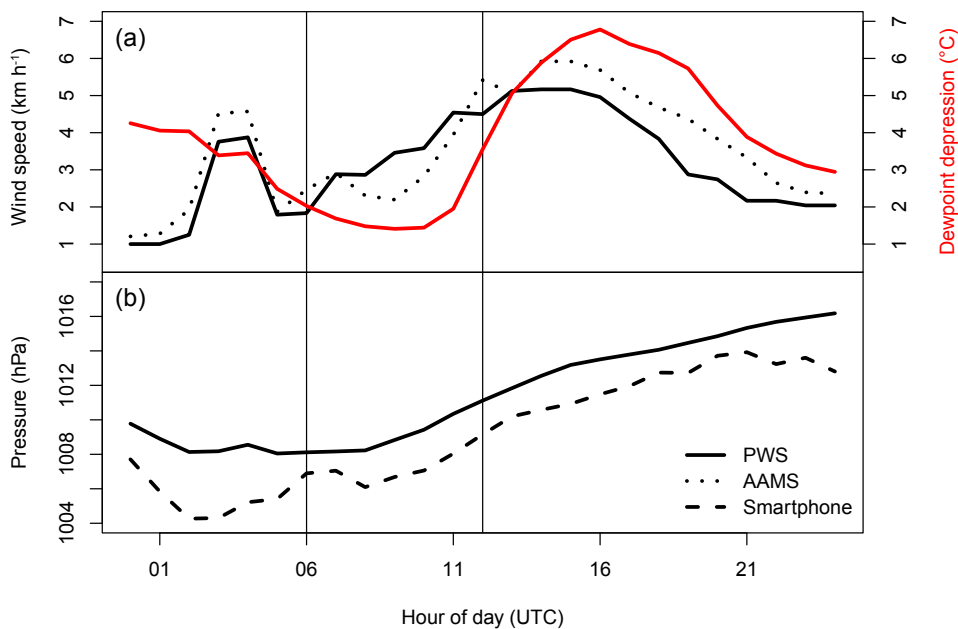
900 the 309 PWSs only 4 are colder than WMO, at most 0.6°C, and 24 are at least 6.0°C warmer
901 than WMO, at most 12.4°C. 50



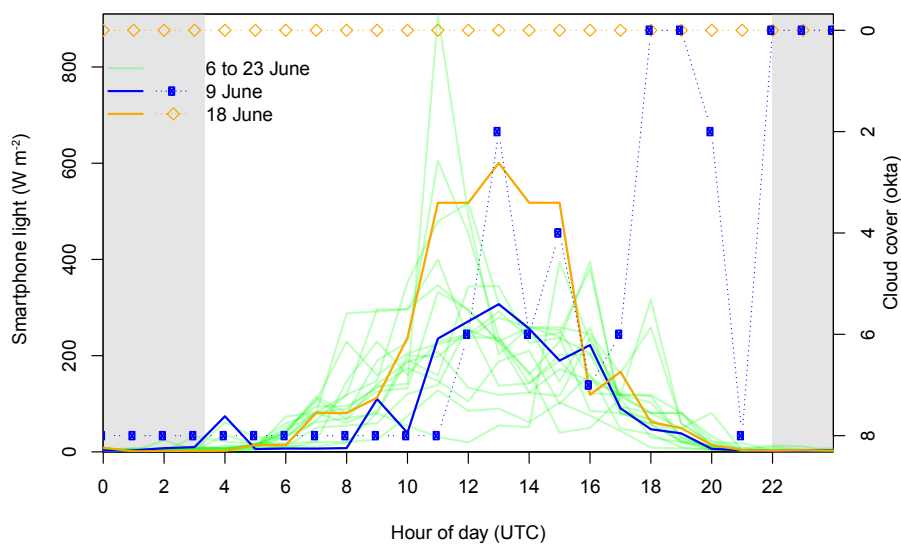
902 FIG. 1. Map of Amsterdam metropolitan area and city center with locations of all sensor networks: Personal
 903 Weather Stations (PWS) and Commercial Microwave Links (CML) (a), and of smartphone battery temperature
 904 readings and Amsterdam Atmospheric Monitoring Supersite (AAMS) stations (b).



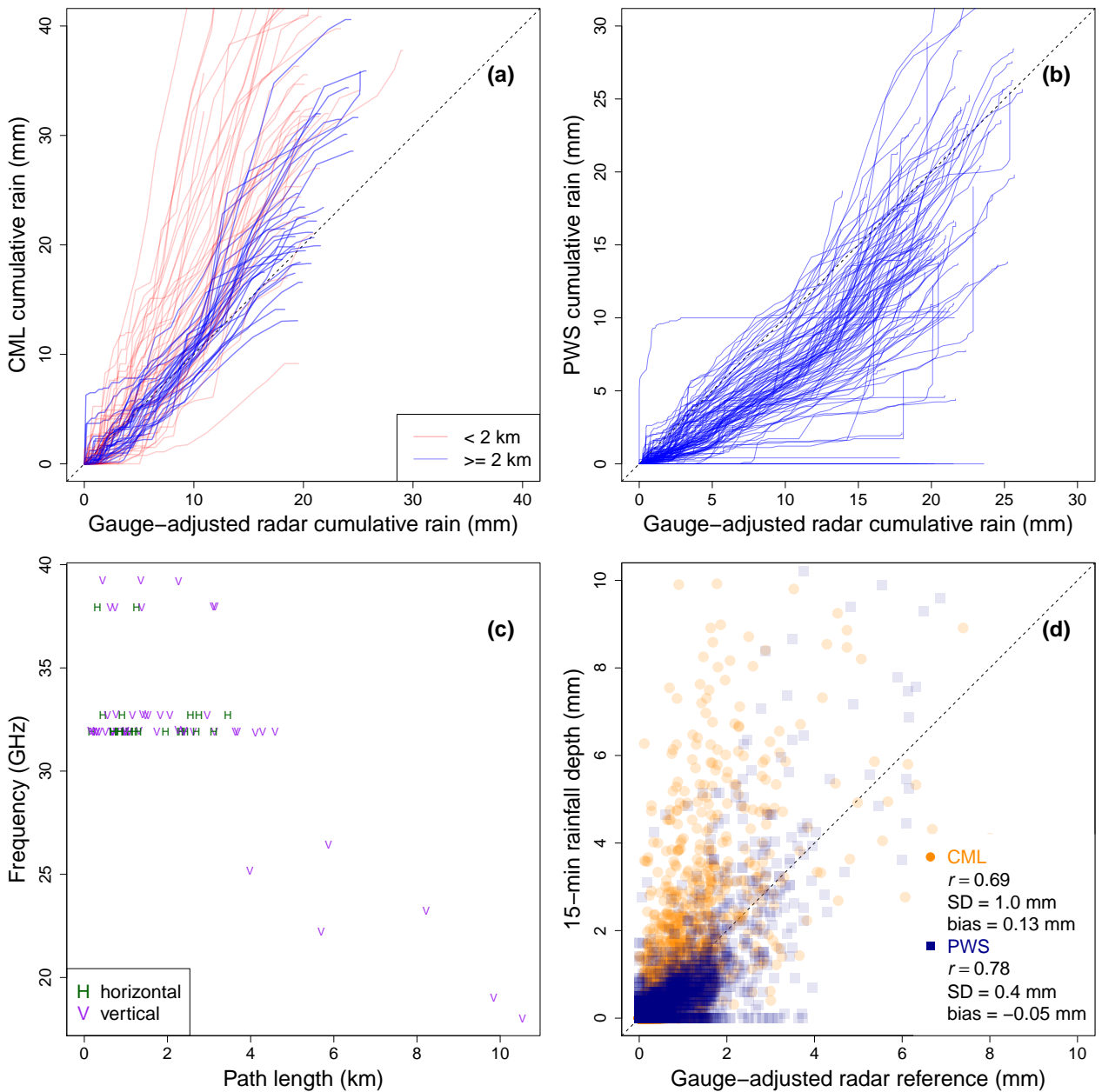
905 FIG. 2. Time series of opportunistic measurements of weather variables. PWS observations of temperature (a),
 906 cumulative rainfall (c), wind (f), pressure (g) and dewpoint depression calculated from humidity and temperature
 907 (i), smartphone battery derived air temperature (b), light (e) and pressure (g). The colored areas indicate the
 908 interquartile range (IQR is mean 25–75 percentile) of all observations at that time; lines show the median values,
 909 except for (b) where the line shows mean temperature. Shaded areas indicate night-time. Pearson correlation
 910 (r), standard deviation of the difference (SD) and absolute bias (bias) are calculated based on hourly values
 911 compared with WMO observations at Schiphol.



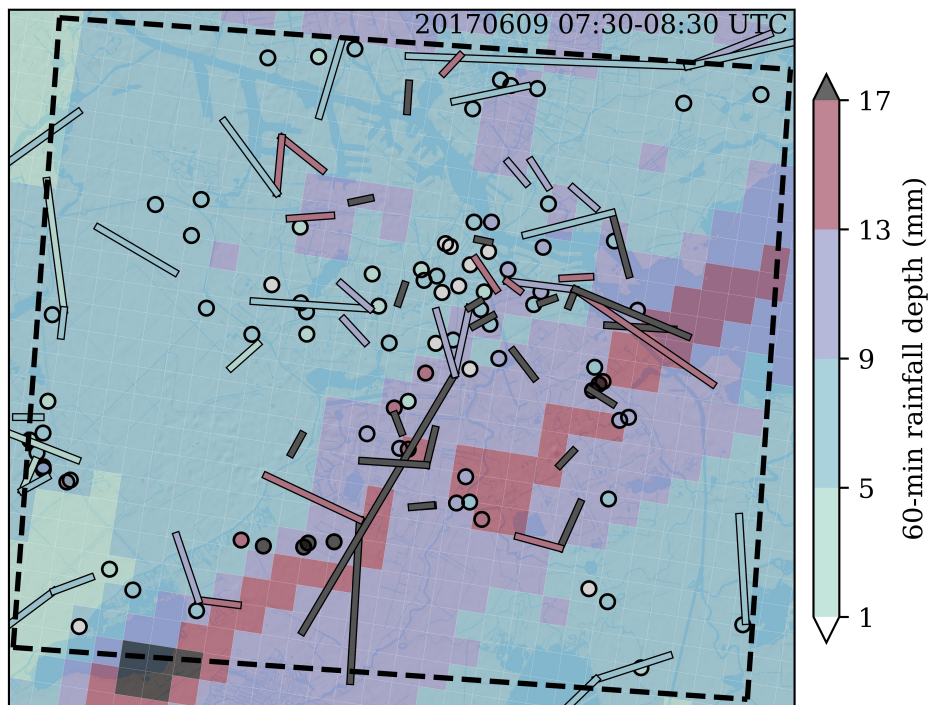
912 FIG. 3. (a) Hourly average wind speed measured by PWS (solid line) and AAMS (dotted line), as well as
 913 the PWS dewpoint depression (red line, right y-axis). (b) Hourly averaged air pressure measured by PWS (solid
 914 line) and smartphone (dashed line) on June 9. The vertical lines indicate the boundaries of the frontal passage.
 915 At 6 UTC the front is located to the west of Amsterdam; at 12 UTC the front has passed over the city.



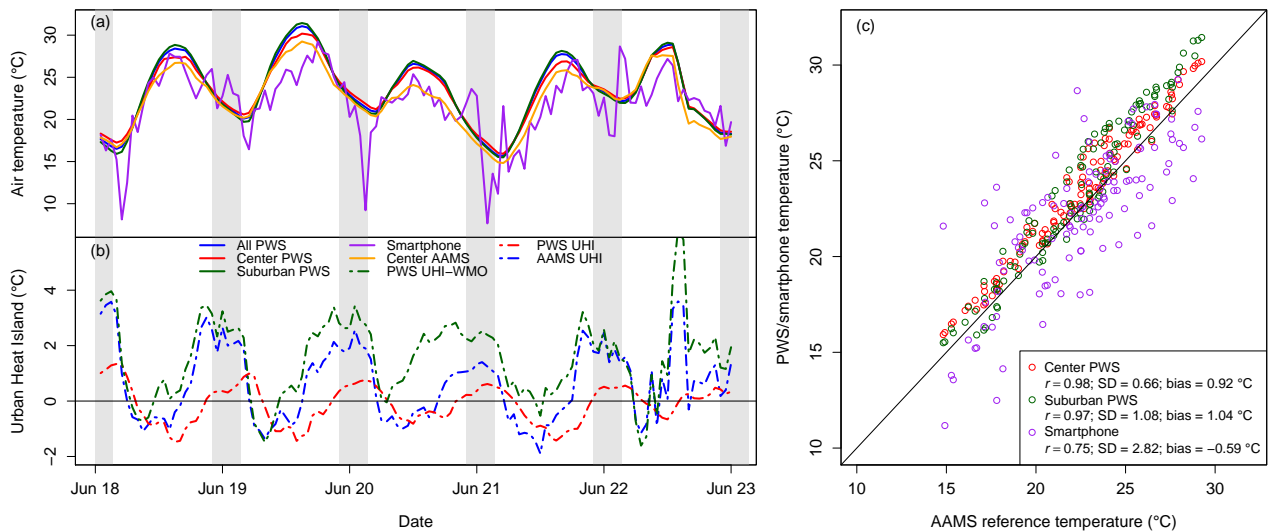
916 FIG. 4. Hourly 99th percentile of smart phone radiation (green lines) with Amsterdam airport cloud cover in
 917 oktas on June 9 (blue, circles) and June 18 (orange, diamonds). June 9 (blue solid line) and June 18 (orange
 918 solid line) are a cloudy and cloud-free day, respectively.



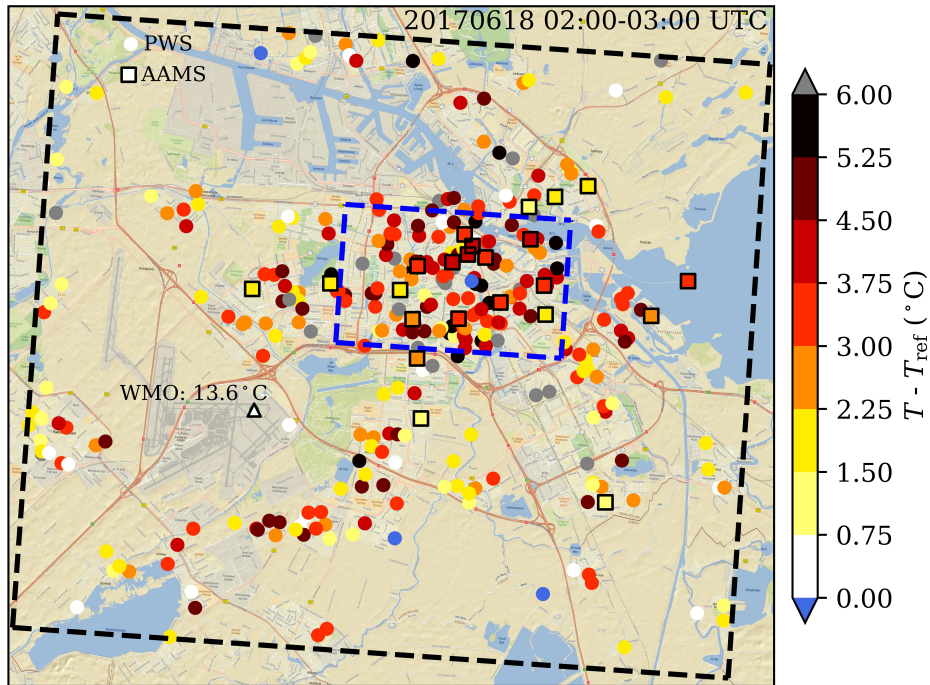
919 FIG. 5. Double mass plots of commercial microwave link derived rainfall observations (a) and PWS rainfall
 920 observations (b) on 9 June against the reference of respectively the path-averaged and overlying pixel gauge-
 921 adjusted radar rainfall observations. Polarization, path length and frequency of the CML network is given in (c)
 922 and (d) shows scatter plots of both together with their Pearson correlation (r), standard deviation of the difference
 923 (SD) and absolute bias (bias) at 15 min time steps.



924 FIG. 6. Map of 60-min rainfall depths over the Amsterdam metropolitan area based on gauge-adjusted radar
 925 data (pixels; 100% availability), CML data (paths; only CMLs with 100% availability are shown), and PWS data
 926 (circles; only PWSs with at least 83.3% availability are shown).



927 FIG. 7. (a) Time series of temperature measurement according to the median of all (blue), center (red) and
 928 suburban (green) PWSs, as well as the median of the AAMS network (orange) and the mean smartphone derived
 929 air temperatures (purple). (b) The difference between the median PWS center and suburban temperatures (red,
 930 dashed); the AAMS and WMO (blue, dashed); and the PWS center and WMO (green, dashed). Shaded areas
 931 indicate night-time. (c) Scatter plot of hourly median PWS and smartphone temperatures against median AAMS
 932 station data, with Pearson correlation (r), standard deviation of the difference (SD) and absolute bias (bias).



933 FIG. 8. Urban Heat Island map for the Amsterdam metropolitan area (black rectangle) showing difference
 934 between hourly averaged air temperature for AAMS network (squares) and PWSs (circles) with respect to 1.5-m
 935 air temperature at WMO station Amsterdam airport observed at 3 UTC (triangle). The blue rectangle represents
 936 Amsterdam city center, the remainder of the metropolitan area is suburban. Only stations with at least 80%
 937 availability are shown. Of the 309 PWSs only 4 are colder than WMO, at most 0.6°C, and 24 are at least 6.0°C
 938 warmer than WMO, at most 12.4°C.